POLITECNICO DI TORINO
Repository ISTITUZIONALE

On the Impact of Large-Scale Vortical Gusts on the Aeroacoustics of a Propeller at Low Reynolds Numbers

Original
On the Impact of Large-Scale Vortical Gusts on the Aeroacoustics of a Propeller at Low Reynolds Numbers / Ali, M., Piccolo, A., Zamponi, R., Ragni, D., Avallone, F.. - (2026). (32nd AIAA/CEAS Aeroacoustics Conference (2026) Brussels (BEL) 26-29 May 2026) [10.2514/6.2026-3338].

Availability:
This version is available at: 11583/3011200 since: 2026-06-15T09:55:20Z

Publisher:
American Institute of Aeronautics and Astronautics

Published
DOI:10.2514/6.2026-3338

Terms of use:

This article is made available under terms and conditions as specified in the corresponding bibliographic description in the repository

Publisher copyright
AIAA preprint/submitted version e/o postprint/Author's Accepted Manuscript

(Article begins on next page)

19 November 2026

On the Impact of Large-Scale Vortical Gusts on the Aeroacoustics of a Propeller at Low Reynolds Numbers

Mario Alì[1], Andrea Piccolo[2], Riccardo Zamponi[2,3], Daniele Ragni[2], and Francesco Avallone[1]
[1]*Department of Mechanical and Aerospace Engineering, Politecnico di Torino, Corso Duca degli Abruzzi 24, Torino, 10129, Italy*
[2]*Department of Aerospace Engineering, Delft University of Technology, Kluyverweg 1, Delft, 2629 HS, The Netherlands*
[3]*Department of Aerospace Engineering, von Karman Institute for Fluid Dynamics, Waterloosesteenweg 72, Sint-Genesius-Rode, B-1640, Belgium*

This study investigates the aeroacoustic behavior of a low-Reynolds-number propeller in forward flight subjected to large-scale inflow disturbances. The incoming flow is modeled as single-frequency sinusoidal vortical gusts, enabling a systematic assessment of the effects of gust frequency, initial phase, and direction on aerodynamic performance and noise generation. The numerical setup is first validated against experimental data under steady inflow conditions. The results show that the loading fluctuations caused by the incoming gust result in discrete tonal components in the acoustic spectrum at frequencies determined by the combination of the gust frequency and multiples of the rotational frequency. These components arise from a double modulation mechanism, and their amplitude is further shaped by inter-blade interference effects. The phase of the gust with respect to the rotor primarily affects the phase of the blade response, thereby modifying the noise directivity, particularly at low frequencies. When the gust is inclined relative to the mean flow, the interaction becomes more complex, leading to a richer tonal spectrum with high intensity tones extending up to the 10th harmonic of the blade passing frequency. Overall, the results provide a physical interpretation of the coupling between rotating blades and large-scale inflow disturbances, supporting the development of improved models for unsteady tonal noise prediction.

Nomenclature

x, y, z	Cartesian coordinates	c_p	Pressure coefficient
R, D	Propeller radius, diameter	J_n	Bessel function of the first kind of order n
Ω	Rotational speed	t	Time
BPF	Blade Passing Frequency	ν	Kinematic viscosity
U_∞	Freestream velocity	ρ	Fluid density
A	Gust amplitude	c_0	Speed of sound
k_x, k_y	Gust longitudinal, transverse wavenumbers	p	Acoustic pressure
ω	Angular frequency	SPL	Sound Pressure Level
f	Frequency	u, v, w	Velocity components in the x, y, z directions
ϕ_0	Initial phase of the gust	$V_{t,\text{eff}}$	Effective tangential velocity
α	Gust direction angle	gust	Gust-related quantity
T, Q	Thrust, torque	rot	Rotational quantity
C_T, C_Q	Thrust, torque coefficients	rms	Root mean square
$c_{f,z}$	Skin-friction coefficient in the chordwise direction		

I. Introduction

In recent years, Urban Air Mobility (UAM) has driven extensive research efforts, with acoustics emerging as a critical factor for public acceptance in densely populated environments [1–3]. A large body of work has investigated the aeroacoustic performance of these systems, focusing on the physical mechanisms of noise generation [4, 5]. The main contributions include thickness noise and loading noise [6, 7]: the former is inherently periodic and mainly tonal [8], while the latter contributes to both tonal and broadband components and is strongly influenced by turbulence and inflow distortions [7, 9].

Urban operating conditions are characterized by multi-scale, highly disturbed inflows originating from atmospheric boundary layers, upstream obstacles, and thermal gradients [10–15]. These conditions are particularly critical for small propellers operating at low Reynolds numbers, which are highly sensitive to inflow perturbations [16].

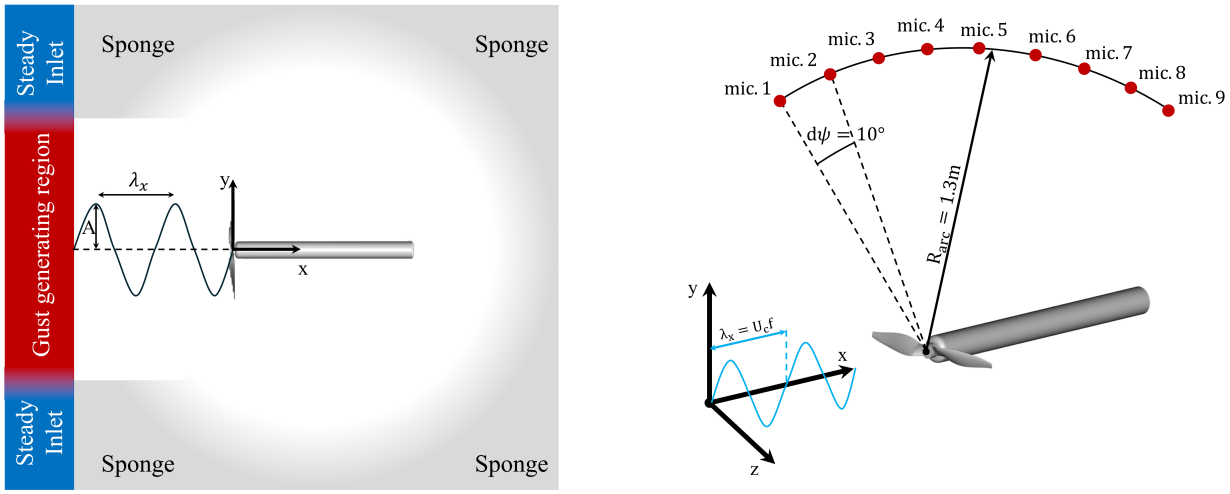
Most investigations into the interaction between propellers and turbulence rely on turbulence grids to generate nearly isotropic inflow conditions [17, 18]. Under such conditions, ingested turbulence primarily increases the broadband noise floor in the mid-frequency range, particularly above the 2nd BPF, while the high-frequency content remains largely unaffected in the presence of a Laminar Separation Bubble (LSB) [19]. These setups typically involve small-scale turbulence.

In contrast, large-scale anisotropic disturbances have been investigated by placing propellers in the wake of bluff bodies, such as cylinders [20–23]. These studies report not only an increase in broadband noise but also the emergence of side peaks around the first harmonic, whose origin remains unclear.

The objective of this work is to quantify the effects of gust scale, phase, and direction on propeller aerodynamics, noise generation mechanisms, and resulting acoustic emissions. The inflow disturbances are modeled as single-frequency harmonic vortical gusts, enabling a controlled and parametric study of their interaction with the low-Reynolds-number propeller, following an approach previously used in airfoil aeroacoustics and wind energy applications [24–28]. Although real inflow turbulence is broadband and stochastic, the use of single-frequency disturbances allows for the isolation of fundamental interaction mechanisms associated with individual spectral components. In this sense, the response to harmonic gusts can be interpreted as a building block of the more complex propeller–turbulence interaction.

Finally, the paper is structured as follows: the numerical setup is described in Sec. II and validated for the clean case in Sec. III; results are discussed in Sec. IV, and conclusions are drawn in Sec. V.

II. Numerical Setup



(a) **(b)**

Fig. 1 (a) Sketch of the numerical setup and (b) microphone positions.

A sketch of the numerical setup is shown in Fig. 1. The streamwise direction is aligned with the x-axis, while u, v, w denote the velocity components along x, y, z, respectively. The propeller, positioned at 15 D downstream of the inlet, is the reference one investigated in previous studies [4, 5]. The rotational speed is $\Omega = 6000\,\mathrm{RPM}$.

The gust, superimposed on the mean velocity $U_\infty = 10\,\mathrm{m\,s^{-1}}$, is introduced via an unsteady inlet boundary condition

following Zhong et al. [25], with velocity components:

$$
\begin{aligned}
u_{\text{gust}}(x,y,t) &= -g(y)h(z)\frac{Ak_y}{\sqrt{k_x^2+k_y^2}}\sin\left(k_x x + k_y y - \omega_{\text{gust}} t\right) + g'(y)h(z)\frac{A}{\sqrt{k_x^2+k_y^2}}\cos\left(k_x x + k_y y - \omega_{\text{gust}} t\right), \\
v_{\text{gust}}(x,y,t) &= g(y)h(z)\frac{Ak_x}{\sqrt{k_x^2+k_y^2}}\sin\left(k_x x + k_y y - \omega_{\text{gust}} t\right), \\
w_{\text{gust}}(x,y,t) &= 0.
\end{aligned}
\tag{1}
$$

Here, A is the gust amplitude, k_x and k_y are the longitudinal and transverse wave numbers, respectively, and $\omega_{\text{gust}} = U_\infty k_x$ is the gust angular frequency. The C_∞ functions $g(y)$ and $h(z)$ confine the gust to a localized inlet region, ensuring smooth transitions between the gust generating area and the rest of the inlet. The second term in the first equation ensures the divergence-free condition, thereby preventing the formation of spurious acoustic waves.

Sponge zones are applied near domain boundaries to reduce reflections, excluding the gust-generating region to avoid damping. Within these zones, the viscosity increases smoothly from its natural level to an imposed one.

The computational grid consists of 15 regions (named *VR*s) with a constant cell (*voxel*) size. Upstream of the propeller, resolution ensures at least 10 voxels per gust wavelength to prevent numerical damping, while refined inner VRs around the propeller capture key flow features [16].

Acoustic predictions at the microphones location (Fig. 1b) are obtained using the solid formulation of the Ffowcs Williams–Hawkings (FWH) analogy [6], applied to the propeller surface and propagated to the far field. Quadrupole sources are neglected due to the low Mach number [7].

In addition to the clean inflow case, five gust configurations (Tab. 1) are considered, varying frequency, phase, and direction. In particular, the phase is examined because the gust is directional, and its impact is expected to vary depending on the direction in which it acts along the blade. The gust amplitude is kept constant at 10% of U_∞.

Gust case	$k_x/2\pi$ [cm^{-1}]	$k_y/2\pi$ [cm^{-1}]	$\text{f}_{\text{gust}}/\text{f}_{\text{rot}}$	ϕ_0 [°]
1	1/10	0	1	0
2	1/15	0	2/3	0
3	1/20	0	1/2	0
4	1/10	0	1	90
5	1/10	1/10	1	0

Table 1 Gust cases tested.

III. Validation for the clean case

In this section, the numerical setup is validated against experimental data for the clean inflow case. A grid independence study for a similar configuration was previously conducted by the authors [19], showing that satisfactory convergence was achieved for the adopted grid resolution ($y^+ \approx 10$). The same grid resolution is used in the present study.

Table 2 compares the thrust and torque coefficients

$$
C_T = \frac{T}{\rho f_{\text{rot}}^2 D^4}, \qquad C_Q = \frac{Q}{\rho f_{\text{rot}}^2 D^5}
\tag{2}
$$

obtained from the numerical simulations against experimental data at the same advance ratio available in the literature [5]. The numerical approach shows good agreement with measurements.

Figure 2 compares the time-averaged surface streamlines with the oil-flow visualization. It can be observed that the main flow features are well captured, although separation and reattachment appear slightly delayed compared to the

	Numerical	Experimental [5]
C_T	0.089	0.09
C_Q	0.0084	0.008

Table 2 Thrust and torque coefficients for the clean inflow condition.

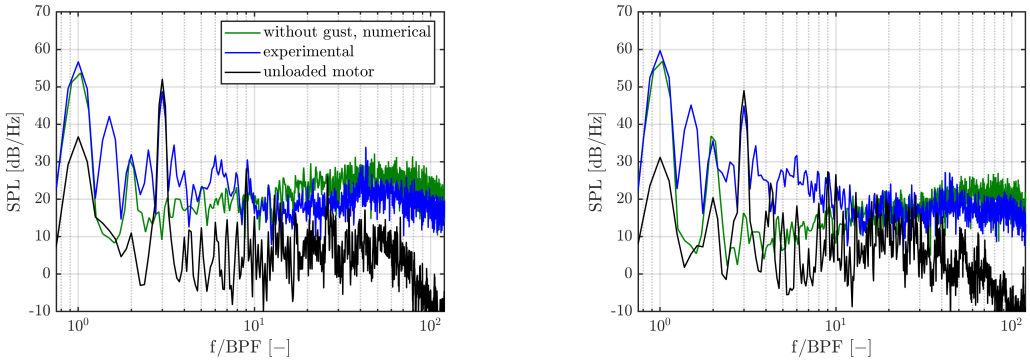


(a) **(b)**

Fig. 2 (a) Time-averaged surface streamlines and (b) oil flow visualization.

experiment, likely due to boundary-layer modeling. In particular, close to the tip region, where the Re is higher, the numerical approach fails to capture the reattachment point.

Figure 3 presents the acoustic spectra at mics. 1 and 4, located outside and within the propeller plane, respectively. Throughout this work, all spectra are reported with respect to the reference pressure is $p_{ref} = 2 \times 10^{-5}$Pa. The first two harmonics are well predicted by the numerical approach. Interharmonic tonal components in the experimental measurements are attributed to slight blade imbalance [16], whereas the experimental 3rd harmonic is dominated by motor noise. At mic. 4, the mid-frequency range is also affected by loaded motor noise [16]. At higher frequencies, where trailing-edge noise dominates [29], the high-fidelity simulation slightly overpredicts the acoustic levels, likely due to small discrepancies in the LSB prediction (Fig. 2). Overall, the agreement between numerical and experimental results is satisfactory, supporting the validity of the numerical approach.



(a) **(b)**

Fig. 3 Acoustic spectra at mics. (a) 1 and (b) 4 for the clean inflow case.

IV. Results and discussion

A. Global overview

This section presents the results on the influence of the gust on the flow development over the blade. $c_{f,z}$ is used to identify the location of the LSB, while $c_{p,rms}$ is employed to highlight where pressure fluctuations are affected by the incoming gust and how they vary with the gust parameters. The detailed parametric study on unsteady loading and far-field noise is reported in Secs. IV.B and IV.C.

In general, the large-scale disturbances considered in this study do not significantly modify the mean flow over the

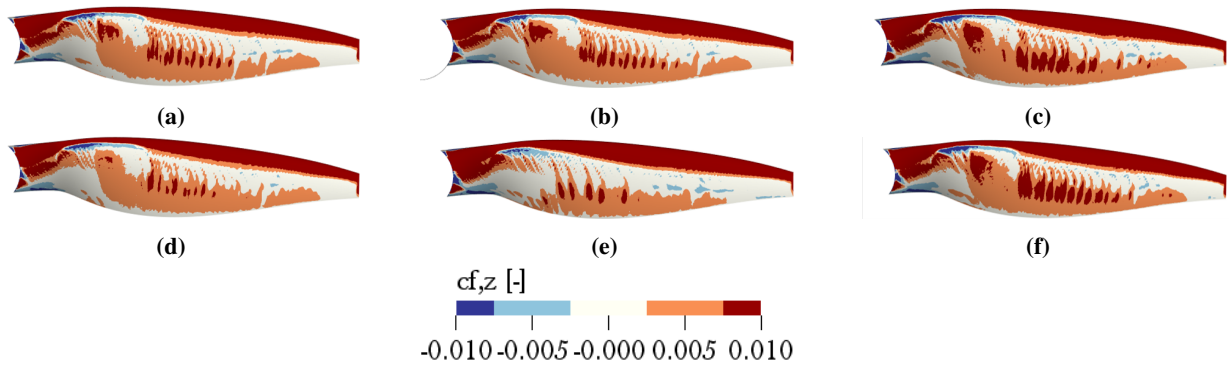


Fig. 4 Mean $c_{f,z}$ on the suction side for the case without gust (a) and for the cases with gust (b–f), the latter corresponding to conditions 1–5 in Tab. 1.

surface. Figure 4 presents the mean $c_{f,z}$, deliberately restricted to a narrow range to better highlight the location and extent of the LSB. The results indicate that the time-averaged location of the LSB shows little sensitivity to variations in gust frequency (Fig. 4b-d). In contrast, the influence of the initial phase is more noticeable (Fig. 4e), where the LSB appears slightly elongated and shifted toward the trailing edge. This effect is particularly pronounced near the tip region, where flow reattachment is not observed. Such behavior is consistent with a slightly lower mean angle of attack. Conversely, the inclined gust leads to a slight increase in skin-friction levels along the reattachment line while leaving the size and position of the LSB largely unchanged.

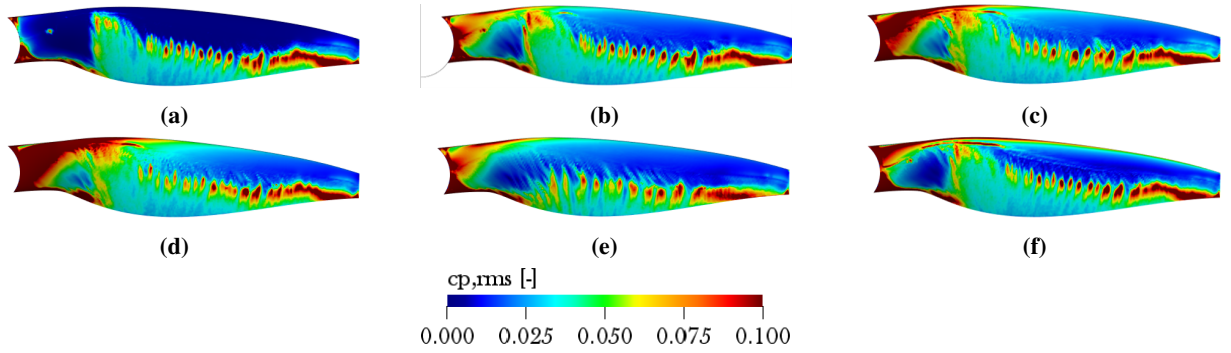


Fig. 5 $c_{p,rms}$ on the suction side for the case without gust (a) and for the cases with gust (b–f), the latter corresponding to conditions 1–5 in Tab. 1.

Figure 5 illustrates the effect of gust interaction on $c_{p,rms}$. In the absence of the gust (Fig. 5a), distinct high-intensity regions are observed along the reattachment line, while upstream areas show virtually no fluctuations, aside from low-level unsteadiness in the tip region across the LSB, likely caused by the tip vortex. When the gust is introduced, pressure fluctuations extend over the entire region from the leading edge to the reattachment line, although the intensity and distribution along the reattachment line remain mostly unchanged. In case 5 (Fig. 5e), the regions of highest fluctuation intensity appear further downstream due to the delayed reattachment discussed earlier. No significant effect on $c_{p,rms}$ is observed when varying the gust parameters. Only a slight increase in fluctuation intensity is noted in the inner region as the gust frequency decreases (Figs. 5b–d), along with a modest enhancement of fluctuations at the leading edge when the gust is inclined relative to the mean flow direction (Fig. 5f).

Finally, Fig. 6 compares the acoustic spectra at mic. 1 for gust cases 1 and 5 with the no-gust condition. The gust has no effect on the first two BPF harmonics, mainly due to steady loading noise, nor on the high-frequency content associated with trailing-edge noise. Similar behavior is observed in all configurations. In contrast, the gust introduces additional tonal noise in the low- to mid-frequency range, extending up to approximately the 10th BPF harmonic for gust case 5. The following analysis will therefore focus on unsteady loading and far-field noise up to the 10th BPF harmonic.

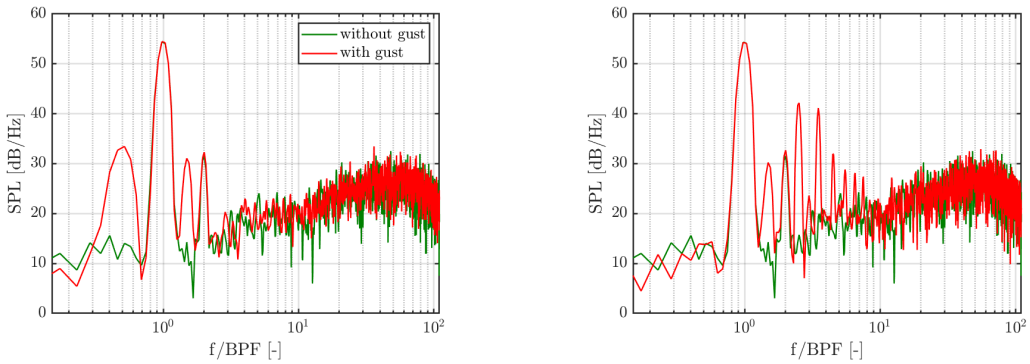


Fig. 6 Comparison of the acoustic spectra at mic.1 without and with gust, for gust cases (a) 1 and (b) 5.

B. Unsteady loading

1. Effect of gust frequency

Here, we analyze the effect of gust frequency on the unsteady loading in the case of spanwise-uniform gusts ($k_y = 0\,\mathrm{cm}^{-1}$), which implies that gusts involve only a fluctuation of the velocity component contained in the propeller plane, while the upwash component is not affected. This is obtained by setting k_y to $0\,\mathrm{cm}^{-1}$ and varying the gust frequency ω_{gust}, and consequently the longitudinal wavenumber k_x.

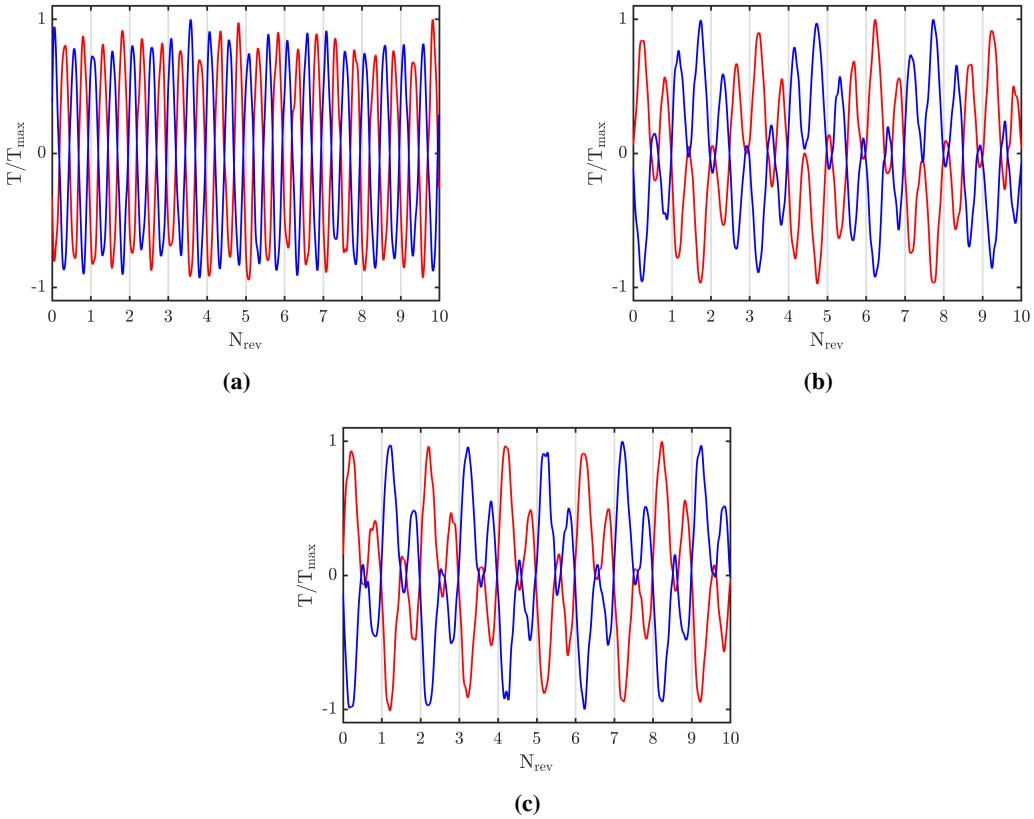


Fig. 7 Effect of f_{gust} on the unsteady loading over the rotor revolutions N_{rev}; (a–c) correspond to cases 1–3 in Tab. 1. The two colors identify the two blades.

Figure 7 shows the time history of the blade thrust for all the analyzed gust frequencies. In all cases, the gust induces fluctuations in the blade loading, associated with the periodic variation of the effective tangential velocity. The loading fluctuations of the two blades are consistently in phase opposition at all frequencies. This occurs because an increase in tangential velocity on one blade corresponds to a simultaneous decrease on the other and, in the linear regime, to a consequent variation of the angle of attack and sectional loading. Such behavior is indicative of large-scale, spatially correlated velocity fluctuations across the propeller disk and would not be expected in the case of small-scale turbulence. As a result, these fluctuations cancel out in the integral thrust and are not visible in the overall unsteady loading. For this reason, the following analysis of the unsteady loading spectrum is performed on a single blade rather than on the entire rotor.

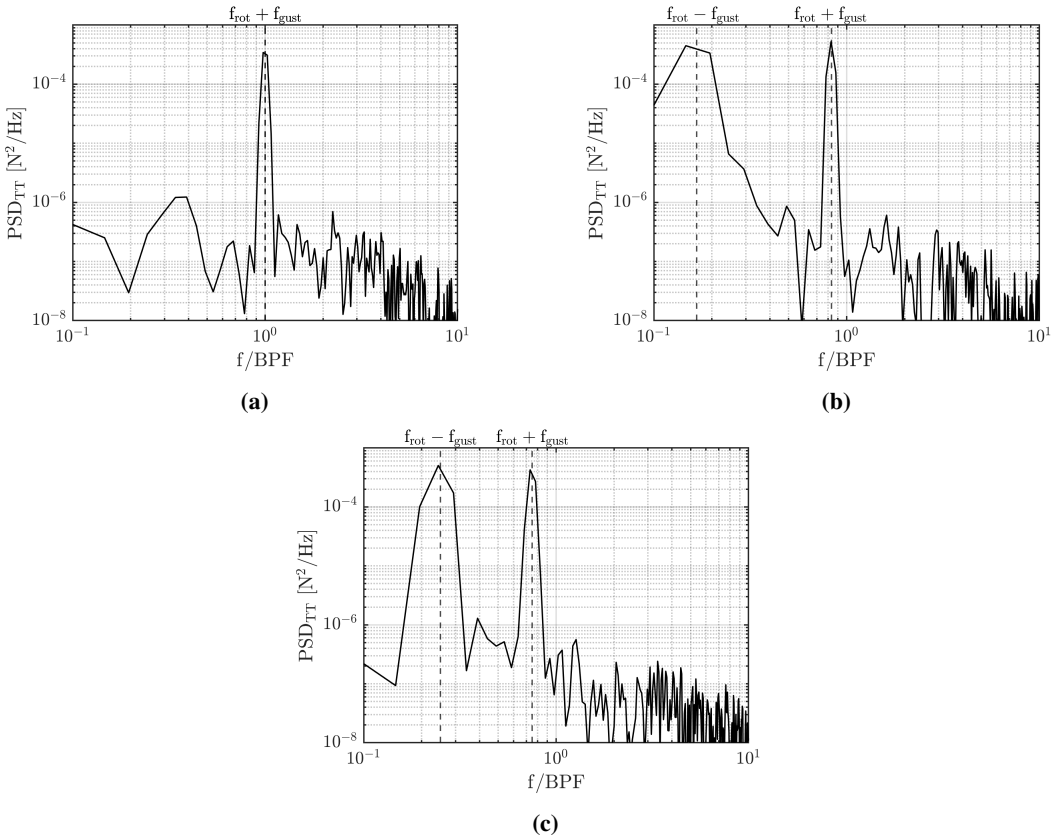


Fig. 8 Effect of f_{gust} on the unsteady loading spectrum for a single blade; (a–c) correspond to cases 1–3 in Tab. 1.

Figure 8 shows the loading spectra for a single blade across all considered gust frequencies. Distinct tonal components emerge in the low-frequency range at $f_{rot} \pm f_{gust}$, indicating that the inflow fluctuations interact with the rotational frequency rather than directly imprinting their own frequency on the unsteady loading, since the gust perturbs only the in-plane velocity component. This will have an impact on the acoustic radiation of the propeller, which will be shown in Sec.IV.C.

2. Effect of gust initial phase

We now explore the effect of the gust initial phase ϕ_0, defined as the propeller phase angle at which the propeller starts to interact with the gust. In general, the initial phase is expected to play a role because the gust is characterized by a specific direction. More specifically, the gust initial phase is examined for the spanwise-uniform gust at frequency $f_{gust}/f_{rot} = 1$, which implies a lock-in effect, meaning that a specific value of the gust-induced velocity perturbation corresponds to a specific propeller phase angle. This can amplify the effect of the initial phase.

Figure 9 illustrates the unsteady loading over one revolution for a gust characterized by $f_{gust}/f_{rot} = 1$, considering two initial phases: $\phi_0 = 0°$ (at which the propeller experiences the highest disturbance along the radial direction) and

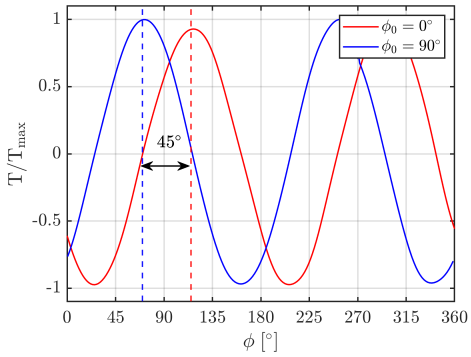


Fig. 9 Effect of the initial phase, ϕ_0, on the phase averaged unsteady loading.

90° (at which the propeller experiences the highest disturbance along the chordwise direction). The resulting time histories exhibit a phase offset of approximately 45°. This shift is consistently reflected in the time derivative of the loading. Given that unsteady loading constitutes a primary source of noise generation, such a phase variation is expected to affect the resulting noise directivity.

3. Effect of gust direction

Here, we illustrate the effect of the gust direction α. The direction of the gust is varied by introducing the transverse wave number k_y, which introduces a periodic fluctuation in the upwash velocity component. However, this also alters the coherence of the angle of attack fluctuations along the blade radius. Here, two directions are examined ($\alpha = 0°$ and 45°) for the frequency $f_{gust}/f_{rot} = 1$.

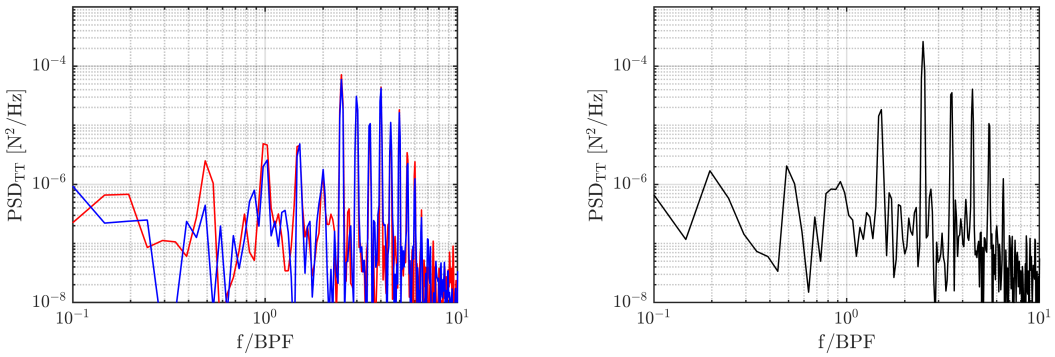


Fig. 10 Effect of gust direction α on the unsteady loading spectrum: (a) per blade and (b) total. The two colors in (a) refer to the two blades.

Figure 10 compares the unsteady loading spectra for gust directions $\alpha = 0°$ and $\alpha = 45°$. When the gust is inclined ($\alpha = 45°$), both in-plane and out-of-plane velocity components are affected, leading to a more complex variation of the angle of attack along the rotor diameter and to an unsteady loading spectrum that is richer in tonal peaks. The individual blade loading (Fig. 10a) shows tones at both BPF harmonics and interharmonics, whereas the total loading (Fig. 10b) contains only interharmonic components. This indicates that fluctuations at BPF harmonics are in phase opposition between the blades and cancel out in the total spectrum. Interestingly, even though the upwash velocity spectrum contains a peak at f_{gust}, only a weak tone is observed in the unsteady loading spectrum at that frequency, whereas higher harmonics are stronger. Likely, this occurs because of a phase difference in the angle of attack fluctuation along the blade radius, which makes the blade-gust interaction more complex. In addition, it is worth mentioning that, in this particular case, BPF interharmonics coincide with condition $f_{gust} + n \times f_{rot}$, with n being even, whereas the harmonics

correspond to cases with n being uneven.

C. Acoustics

1. *Effect of gust frequency*

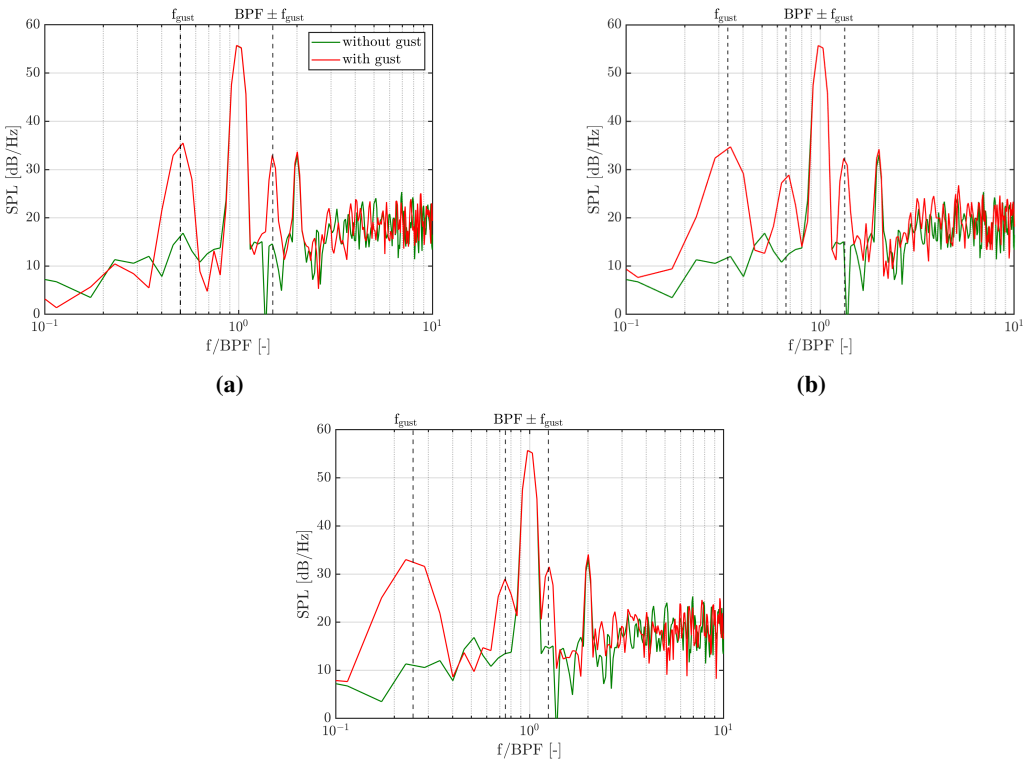


Fig. 11 Effect of f_{gust} on the acoustic spectrum at mic. 1; (a–c) correspond to cases 1–3 in Tab. 1.

We now analyze how variations in gust frequency for spanwise-uniform gusts ($k_y = 0\,\mathrm{cm}^{-1}$), previously discussed in relation to the unsteady loading, affect the far-field noise..

Figure 11 compares the acoustic spectra at mic. 1 for gust cases 1-3 in Tab.1 against the clean configuration. The first two harmonics, mostly determined by steady loading and thickness noise, remain unchanged. However, additional tonal components consistently appear at f_{gust} and BPF $\pm$ f_{gust}, indicating a nonlinear interaction between the gust and the blade passing frequency. Similar features have been reported in propeller–wake interaction studies [21, 23], suggesting a common underlying mechanism. Notably, the propeller is the sole acoustic source at f_{gust}, as the vortical gust itself does not radiate sound. It will be shown in Sec. IV.D that these tonal peaks are a direct consequence of the peaks observed in the unsteady loading spectra (Fig. 8). In particular, they result from the amplitude modulation of the unsteady loading caused by blade rotation.

2. *Effect of initial phase*

Figure 12 shows the effect of ϕ_0 on the acoustic spectrum at mic. 1 for $f_{gust}/f_{rot} = 1$. Consistent with the observation on the unsteady loading in Fig.9, both configurations exhibit the same additional tonal components. However, a slight reduction in the amplitude of the peak at BPF $-$ f_{gust} is observed for $\phi_0 = 0°$, suggesting a modification of the directivity pattern. In contrast, the additional tone at BPF + f_{gust} does not exhibit any influence.

This effect is further clarified in Fig. 13, which presents the directivity of the tones at BPF $\pm$ f_{gust}. The influence of ϕ_0 is more pronounced at BPF $-$ f_{gust}, where the Sound Pressure Level (SPL) decreases and the directivity pattern rotates for $\phi_0 = 0°$ compared to $\phi_0 = 90°$. For $\phi_0 = 90°$, the radiation is strongest along the velocity fluctuation direction,

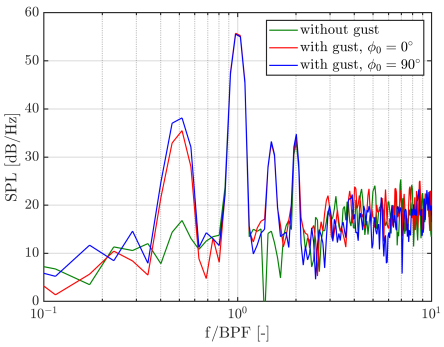


Fig. 12 Effect of the initial phase of the gust on acoustic spectrum at mic. 1.

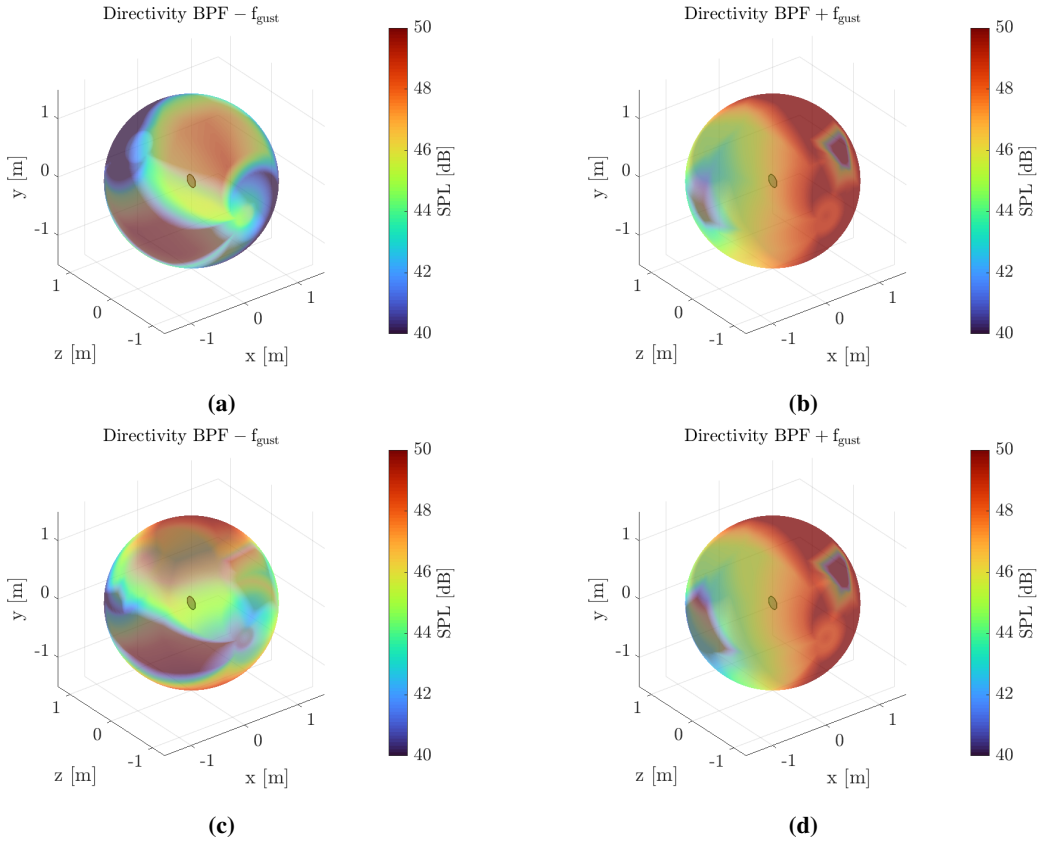


Fig. 13 Directivity of the peaks at BPF ± f_{gust} **for (a,b)** $\phi_0 = 0°$ **and (c,d)** $\phi_0 = 90°$**. The disk shown at the center of each subfigure represents the propeller disk. The gust acts along the** y**-direction.**

whereas for $\phi_0 = 0°$ it is weaker and shifted opposite to the propeller rotation. In contrast, the case for BPF + f_{gust} shows similar levels and spatial distributions for both phases, with higher intensity downstream of the propeller. In general, the initial phase affects the directivity of tonal noise, particularly at lower frequencies, thereby explaining the difference in the noise level at BPF − f_{gust} observed in Fig.12. This effect is expected to be amplified here since $f_{gust} = f_{rot}$, so the blade encounters identical inflow conditions at each revolution.

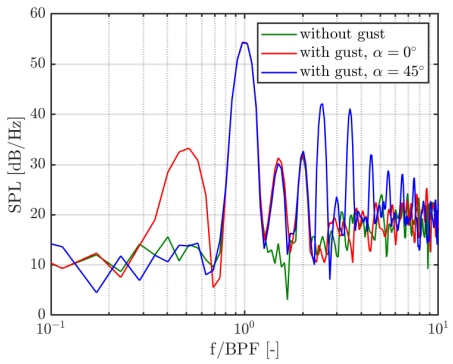


Fig. 14 Effect of gust direction on acoustic spectrum at mic. 1.

3. Effect of gust direction

Figure 14 shows the acoustic spectra at mic. 1 for clean inflow and cases 1 and 5 in Tab. 1. When the gust is inclined relative to the mean flow, e.g., $\alpha = 45°$, a richer tonal spectrum with peaks up to the 10th BPF harmonic is observed. Except for the 1st and 2nd BPF harmonics, only interharmonic peaks are observed. Again, similar to the unsteady loading spectrum, no peak appears at f_{gust}, although the upwash velocity spectrum contains that frequency. The next section shows that this is caused by a destructive interference at $f = f_{gust}$ between the acoustic waves radiated by the two blades.

D. Interpretation of the results

1. Unsteady loading

The vortical gust affects the blade angle of attack and unsteady loading through two mechanisms, depending on its direction: modulation of the effective tangential velocity or perturbation of the upwash velocity. Here, the effects of normal and planar disturbances on loading and acoustics are considered, neglecting distortions from the propeller-induced mean flow.

The blade is modeled as a rotating point with radius r in the yz-plane at an angular frequency ω_{rot}. With $y(t) = r\sin(\omega_{rot}t + \phi_0)$, the gust velocity components at the propeller plane become:

$$\begin{aligned} u_{gust}(r,t) &= -\frac{Ak_y}{\sqrt{k_x^2 + k_y^2}} s(r,t), \\ v_{gust}(r,t) &= \frac{Ak_x}{\sqrt{k_x^2 + k_y^2}} s(r,t), \end{aligned} \tag{3}$$

having defined

$$s(r,t) = \sin\left[k_y r \sin(\omega_{rot}t + \phi_0) - \omega_{gust}t\right]. \tag{4}$$

Blade rotation introduces frequency modulation, and $s(r,t)$ can be expanded as:

$$s(r,t) = \sum_{n=-\infty}^{\infty} J_n(k_y r)\sin\left[(n\omega_{rot} - \omega_{gust})t + n\phi_0\right], \tag{5}$$

yielding spectral peaks at:

$$\omega = n\omega_{rot} - \omega_{gust}, \qquad \text{with } n = -\infty, \ldots, +\infty. \tag{6}$$

In the rotating frame, the effective tangential velocity, given by the sum of the tangential velocity and the gust velocity projected in the tangential direction (Fig. 15), undergoes both phase and amplitude modulation:

$$V_{t,\text{eff}}(t) = \Omega r + \frac{Ak_x}{\sqrt{k_x^2 + k_y^2}}\left[\sum_{n=-\infty}^{\infty} J_n(k_y r)\sin\left((n\omega_{rot} - \omega_{gust})t + n\phi_0\right)\right]\cos(\omega_{rot}t + \phi_0), \tag{7}$$

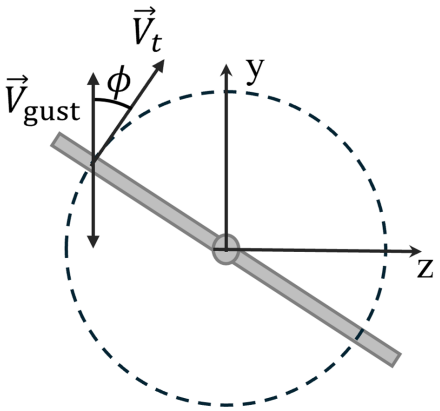


Fig. 15 Modulation of the effective tangential velocity $V_{t,\text{eff}}$.

with spectral peaks at:

$$\omega = (n \pm 1)\omega_{\text{rot}} - \omega_{\text{gust}}. \tag{8}$$

Peak amplitudes depend on combinations of $J_n(k_y r)$ contributing to the specific frequency. In the limit $k_y r \to 0$ (in the case of span-uniform gust), $u_{\text{gust}} = 0\,\text{m}\,\text{s}^{-1}$ and

$$V_{t,\text{eff}}(t) = \Omega r - \frac{A k_x}{\sqrt{k_x^2 + k_y^2}} \sin(\omega_{\text{gust}} t) \cos(\omega_{\text{rot}} t + \phi_0), \tag{9}$$

corresponding to a pure amplitude modulation, with a discrete spectrum at frequencies $\omega_{\text{rot}} \pm \omega_{\text{gust}}$. The discrete frequencies are directly transferred to the blade loading through the induced unsteady variation of the angle of attack. In fact, the gust-induced velocity components modify the relative velocity seen by the blade, producing a perturbation of the angle of attack that contains the same spectral content. Under linear aerodynamic assumptions, the unsteady lift response is linked to the angle of attack through the Theodorsen complex function, so that the loading inherits the same frequency components [30, 31]. This shows that the peaks observed in the unsteady loading spectra arise from the amplitude and phase modulation of the angle of attack. In particular, the peaks in unsteady loading spectra when $k_y = 0\,\text{cm}^{-1}$ arise from the amplitude modulation of the effective tangential velocity induced by the gust.

2. Acoustics

The origin of the tonal noise induced by the gust can be interpreted using Lowson's theory [32], relating it to the unsteady loading spectrum. Indeed, approximating a blade with an equivalent rotating force $\vec{F} = (F_1, F_2, F_3)$, the resulting far-field acoustic pressure is given by:

$$p(\vec{\mathbf{x}}, t) = \left[\frac{(x_i - y_i)}{4\pi a_0 r^2 (1 - M_r)^2} \left(\frac{\partial F_i}{\partial t} + \frac{F_i}{1 - M_r} \frac{\partial M_r}{\partial t} \right) \right]_{t=\tau_1} \tag{10}$$

Here, x_i and y_i denote the ith coordinates of the source and observer, respectively, M_r is the relative Mach number of the source with respect to the observer, and r is their separation distance (Fig. 16). Equation 10 is evaluated at the retarded time $\tau = t - r/a_0$, corresponding to the emission time of the acoustic wave. Since the additional tonal components arise only in the presence of the gust, it is reasonable to attribute them to the unsteady loading term $\partial F_i/\partial t$, while the steady-motion contribution can be neglected. This is confirmed in Fig. 17, which reports the contributions of both terms. The equivalent rotating dipole is placed at 60% of the tip radius, corresponding to the location where the total drag produces the same torque. The FWH-based spectrum is included as a reference. Lowson's model accurately predicts the 1st BPF, with minor discrepancies likely due to the neglect of thickness noise. The 2nd BPF harmonic, mainly associated with steady loading noise, is instead underpredicted because the model does not fully capture the steady loading contribution. Nevertheless, the additional harmonics induced by unsteady loading are well captured, supporting the use of Lowson's model for interpreting the results. In what follows, subscripts 1 and 2 indicate the terms for the two blades.

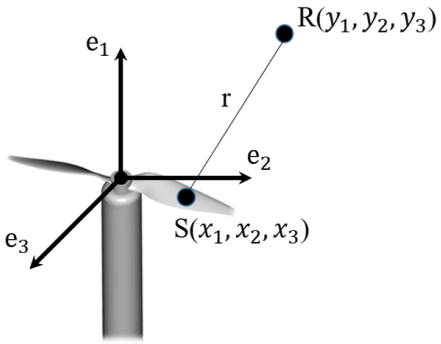


Fig. 16 Absolute frame of reference used in the theoretical analysis. $\mathrm{S}(\mathrm{x}_1, \mathrm{x}_2, \mathrm{x}_3)$ **denotes the source point, while** $\mathrm{R}(\mathrm{y}_1, \mathrm{y}_2, \mathrm{y}_3)$ **is the receiver.**

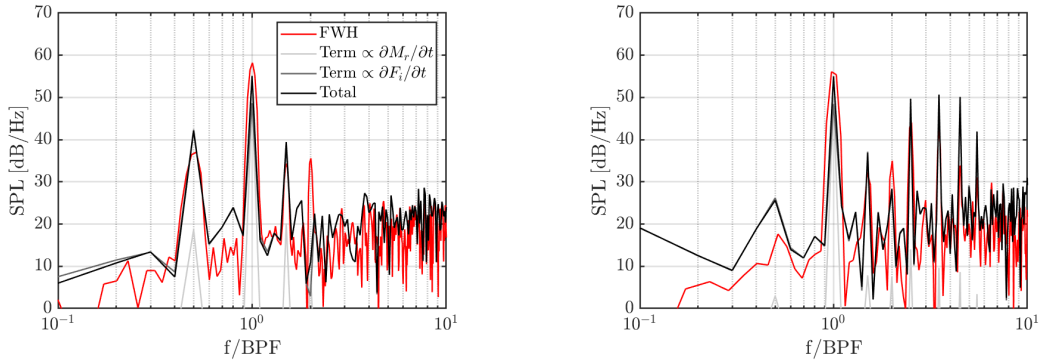


Fig. 17 Contributions of terms in Eq. 10 to the acoustic spectrum at mic.1 for gust cases (a) 1 and (b) 5.

Since in rotational motion, the term expressing the relative position and distance of source 1 with respect to the observer can be expressed as a periodic Fourier series with a fundamental frequency ω_{rot}:

$$q_1(t) = \frac{(x_{1i} - y_i)}{4\pi a_0 r_1^2 (1 - M_{1r})^2} = \sum_{n=-\infty}^{\infty} \hat{q}_n \mathrm{e}^{jn\omega_{\mathrm{rot}}t}. \tag{11}$$

In addition, by expressing the unsteady loading as a Fourier series, where ω_λ represents the λth harmonic in the unsteady loading spectrum:

$$F_{1i} = \sum_{\lambda=1}^{N_h} \hat{F}_{1i,\lambda} \mathrm{e}^{j\omega_\lambda t} \quad \text{and} \quad \frac{\partial F_{1i}}{\partial t} = \sum_{\lambda=1}^{N_h} j\omega_\lambda \hat{F}_{1i,\lambda} \mathrm{e}^{j\omega_\lambda t}, \tag{12}$$

where N_h is the number of unsteady loading harmonics. Then, the acoustic pressure at the receiver at the reception time t due to a single rotating dipole emitting at the retarded time τ_1 can be written as

$$p_1(\vec{\mathbf{x}}, t) \sim \sum_n \sum_\lambda \hat{q}_n \hat{F}_{1i,\lambda} \, \mathrm{e}^{j(\omega_\lambda + n\omega_{\mathrm{rot}})\tau_1}, \tag{13}$$

leading to discrete acoustic frequencies

$$\omega = \omega_\lambda + n\omega_{\mathrm{rot}}. \tag{14}$$

The total acoustic field results from the interference of the contributions of each blade. Since the second blade is rotated by 180°, the ratio $q_2(t)$ can be written as

$$q_2(t) = q_1\left(t + \frac{\pi}{\omega_{\mathrm{rot}}}\right) = \sum_{n=-\infty}^{\infty} \hat{q}_n \mathrm{e}^{j(n\omega_{\mathrm{rot}}t + n\pi)}, \tag{15}$$

whereas the unsteady loading at the same retarded time τ can be written as

$$F_{2i} = \sum_{\lambda=1}^{N_h} \hat{F}_{2i,\lambda} e^{j\omega_\lambda t + \varphi_\lambda} \quad \text{and} \quad \frac{\partial F_{2i}}{\partial t} = \sum_{\lambda=1}^{N_h} j\omega_\lambda \hat{F}_{2i,\lambda} e^{j\omega_\lambda t + \varphi_\lambda}, \tag{16}$$

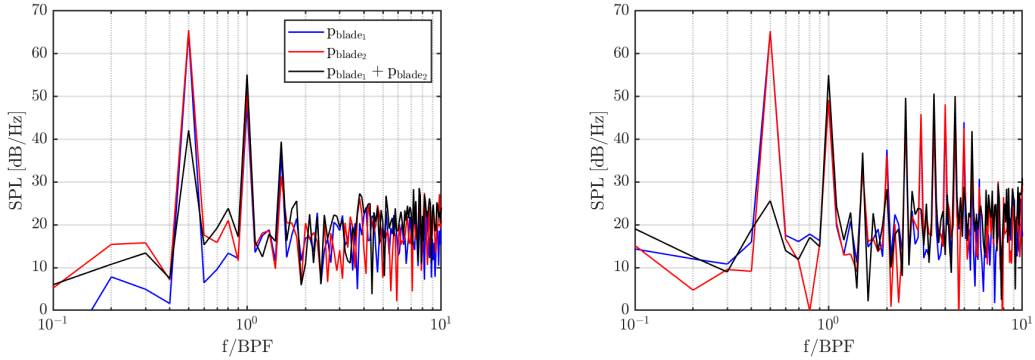
and the acoustic wave from the second source can be expressed as

$$p_2(\vec{\mathbf{x}}, t) \sim \sum_n \sum_\lambda \hat{q}_n \hat{F}_{2i,\lambda}\, e^{j(\omega_\lambda + n\omega_{\text{rot}})(\tau_1 + \Delta\tau)}, \tag{17}$$

where $\Delta\tau$ is the difference between the retarded times of the two dipoles. Then, the overall acoustic wave can be written as

$$p(\vec{\mathbf{x}}, t) \sim \left[\sum_{n=-\infty}^{\infty} \sum_{\lambda=1}^{N_h} j\omega_\lambda \hat{q}_n \hat{F}_{1i,\lambda} e^{j(\omega_\lambda + n\omega_{\text{rot}})t} \left(1 + (-1)^n \frac{\hat{F}_{2i,\lambda}}{\hat{F}_{1i,\lambda}} e^{j[\varphi_\lambda + (\omega_\lambda + n\omega_{\text{rot}})\Delta\tau]} \right) \right]_{t=\tau}. \tag{18}$$

The interference factor depends on the ratio of the λth Fourier coefficients of the blade loading, as well as the phase differences φ_λ and $\Delta\tau$, and determines which multiples of the rotational frequency combine constructively in the resulting acoustic signal.



(a) **(b)**

Fig. 18 Contribution of each blade to the acoustic spectrum at mic. 1, as predicted by Lowson's model, for gust cases (a) 1 and (b) 5.

Figure 18 illustrates this behavior for gust cases 1 and 5. In particular, recalling that for gust 1, the unsteady loading frequencies are

$$\omega_\lambda = \omega_{\text{rot}} \pm \omega_{\text{gust}}, \tag{19}$$

then the acoustic radiated frequencies are

$$\omega = 2\omega_{\text{rot}} \pm \omega_{\text{gust}} = \text{BPF} \pm \omega_{\text{gust}}, \tag{20}$$

which shows that the side-peaks around the 1st BPF are due to the double-modulation mechanism, occurring first in the blade-gust interaction and then in the acoustic emission. Finally, for gust 5, a near-complete cancellation is observed at ω_{gust} and at frequencies $\omega = n\omega_{\text{rot}} + \omega_{\text{gust}}$ for odd values of n.

V. Conclusion

This study numerically investigates, using high-fidelity simulations, the interaction between a low-Reynolds-number propeller and a single-frequency vortical gust, representative of flows generated by vortex shedding from bodies such as cylinders or buildings. The aim is to assess the effects of gust wavelength, phase, and direction on the aeroacoustic response of the propeller.

Overall, additional tonal components arise in the unsteady loading spectrum from interactions between the rotational and gust frequencies. Phase differences between the blades lead to instantaneous loading imbalances. From an acoustic

perspective, these components are radiated at discrete frequencies given by the combination of the gust frequency and multiples of the rotational frequency, with their amplitudes further shaped by interference effects. The present results show that the side-band tones observed in propeller–wake interaction are not the direct signature of the inflow disturbance, but rather the outcome of a two-step modulation process involving blade rotation and acoustic radiation, combined with inter-blade interference effects.

Spanwise-uniform gusts induce amplitude modulation of the tangential velocity and blade loading, generating tones at $f_{rot} \pm f_{gust}$ (in phase opposition between blades), which are radiated at BPF $\pm f_{gust}$ and f_{gust}. The gust initial phase affects the loading phase and thus the noise directivity, especially at low frequencies. Finally, when the gust is inclined with respect to the mean velocity, multiple peaks are observed in the unsteady loading spectrum, influencing the acoustic tonal content up to the 10th BPF harmonic.

The results contribute to a deeper understanding of the interaction between large-scale gusts, particularly flows with periodic phenomena such as vortex shedding, and rotating blades, supporting the development of improved models for unsteady tonal noise prediction.

Acknowledgment

The authors wish to thank Fondazione Compagnia di San Paolo for funding and supporting the present project.

References

[1] Sengupta, R., Bulusu, V., Mballo, C. E., Onat, E. B., and Cao, S., "Urban air mobility research challenges and opportunities," *Annual Review of Control, Robotics, and Autonomous Systems*, Vol. 8, 2025.

[2] Yedavalli, P., and Mooberry, J., "An assessment of public perception of urban air mobility (UAM)," *Airbus UTM: Defining Future Skies*, 2019, pp. 2046738072–1580045281.

[3] Bauer, M. W., Bartels, S., and Redmann, D., "UAM Community Noise Impact Studies," *Proceedings of the Quiet Drones 2024*, 2024.

[4] Casalino, D., Grande, E., Romani, G., Ragni, D., and Avallone, F., "Definition of a benchmark for low Reynolds number propeller aeroacoustics," *Aerospace Science and Technology*, Vol. 113, 2021, p. 106707.

[5] Grande, E., Romani, G., Ragni, D., Avallone, F., and Casalino, D., "Aeroacoustic investigation of a propeller operating at low Reynolds numbers," *AIAA Journal*, Vol. 60, No. 2, 2022, pp. 860–871.

[6] Ffowcs Williams, J. E., and Hawkings, D. L., "Sound generation by turbulence and surfaces in arbitrary motion," *Philosophical Transactions of the Royal Society of London. Series A, Mathematical and Physical Sciences*, Vol. 264, No. 1151, 1969, pp. 321–342. https://doi.org/10.1098/rsta.1969.0031.

[7] Glegg, S., and Devenport, W., *Aeroacoustics of low Mach number flows: fundamentals, analysis, and measurement*, Academic Press, 2017.

[8] Williams, J. F., and Hawkings, D., "Theory relating to the noise of rotating machinery," *Journal of Sound and Vibration*, Vol. 10, No. 1, 1969, pp. 10–21.

[9] Piccolo, A., Zamponi, R., Avallone, F., and Ragni, D., "Modification of Amiet's model for turbulence-ingestion noise prediction in rotors," *The Journal of the Acoustical Society of America*, Vol. 158, No. 1, 2025, pp. 461–475. https://doi.org/10.1121/10.0037185.

[10] Kaimal, J. C., and Finnigan, J. J., *Atmospheric boundary layer flows: their structure and measurement*, Oxford university press, 1994.

[11] Monin, A., "The atmospheric boundary layer," *Annual Review of Fluid Mechanics*, Vol. 2, No. 1, 1970, pp. 225–250.

[12] Liu, J., Niu, J., Mak, C. M., and Xia, Q., "Detached eddy simulation of pedestrian-level wind and gust around an elevated building," *Building and Environment*, Vol. 125, 2017, pp. 168–179.

[13] Park, S.-B., Baik, J.-J., and Han, B.-S., "Large-eddy simulation of turbulent flow in a densely built-up urban area," *Environmental Fluid Mechanics*, Vol. 15, No. 2, 2015, pp. 235–250.

[14] Oke, T. R., "Urban environments," *The surface climates of Canada*, 1997, pp. 303–327.

[15] Priestley, C., "Temperature fluctuations in the atmospheric boundary layer," *Journal of Fluid Mechanics*, Vol. 7, No. 3, 1960, pp. 375–384.

[16] Casalino, D., Romani, G., Zhang, R., and Chen, H., "Lattice-Boltzmann calculations of rotor aeroacoustics in transitional boundary layer regime," *Aerospace Science and Technology*, Vol. 130, 2022, p. 107953.

[17] Jamaluddin, N. S., Celik, A., Baskaran, K., Rezgui, D., and Azarpeyvand, M., "Aeroacoustic performance of propellers in turbulent flow," *AIAA Aviation 2021 Forum*, 2021, p. 2188.

[18] Go, S. T., Kingan, M. J., Bowen, L., and Azarpeyvand, M., "Noise of a shrouded propeller due to ingestion of grid-generated turbulence," *Journal of Sound and Vibration*, Vol. 571, 2024, p. 118044.

[19] Alì, M., Piccolo, A., Zamponi, R., Ragni, D., and Avallone, F., "On the aeroacoustics of a propeller at low Reynolds number subjected to a grid-induced turbulent inflow," *Aerospace Science and Technology*, 2026, p. 112114.

[20] Glegg, S. A., Grant, J., Devenport, W. J., and Alexander, W. N., "Sound Radiation from a Rotor Operating in the Wake of a Cylinder," *55th AIAA Aerospace Sciences Meeting*, 2017, p. 1172.

[21] Trascinelli, L., Romani, G., Hanson, L., Casalino, D., Zang, B., Zhou, B. Y., and Azarpeyvand, M., "Numerical simulations of large-scale turbulence ingestion by a forward flight propeller," *The Journal of the Acoustical Society of America*, Vol. 158, No. 1, 2025, pp. 826–837. https://doi.org/10.1121/10.0037219.

[22] Hanson, L. P., Zang, B., and Azarpeyvand, M., "Experimental Characterisation of Cylinder-Induced Turbulence Ingestion in Propellers Operating in Edgewise Flight," *30th AIAA/CEAS Aeroacoustics Conference (2024)*, 2024, p. 3100.

[23] Yauwenas, Y., Fischer, J. R., Moreau, D., and Doolan, C. J., "The effect of inflow disturbance on drone propeller noise," *25th AIAA/CEAS Aeroacoustics Conference*, 2019, p. 2663.

[24] Gill, J. R., Zhang, X., and Joseph, P., "Effects of real airfoil geometry on leading edge gust interaction noise," *19th AIAA/CEAS Aeroacoustics Conference*, 2013, p. 2203.

[25] Zhong, S., Zhang, X., Gill, J., Fattah, R., and Sun, Y., "A numerical investigation of the airfoil-gust interaction noise in transonic flows: Acoustic processes," *Journal of Sound and Vibration*, Vol. 425, 2018, pp. 239–256.

[26] Yu, H., Shao, M., and Jiang, H., "Numerical study on the time-harmonic gust response of a vertical axis wind turbine," *Physics of Fluids*, Vol. 37, No. 1, 2025.

[27] Danao, L. A., Edwards, J., Eboibi, O., and Howell, R., "A numerical investigation into the influence of unsteady wind on the performance and aerodynamics of a vertical axis wind turbine," *Applied Energy*, Vol. 116, 2014, pp. 111–124.

[28] Wu, Z., "Rotor power performance and flow physics in lateral sinusoidal gusts," *Energy*, Vol. 176, 2019, pp. 917–928.

[29] Grande, E., Ragni, D., Avallone, F., and Casalino, D., "Laminar separation bubble noise on a propeller operating at low Reynolds numbers," *AIAA Journal*, Vol. 60, No. 9, 2022, pp. 5324–5335.

[30] Sears, W. R., "Some aspects of non-stationary airfoil theory and its practical application," *Journal of the Aeronautical Sciences*, Vol. 8, No. 3, 1941, pp. 104–108.

[31] Gülçat, Ü., *Fundamentals of modern unsteady aerodynamics*, Vol. 2010, Springer, 2010.

[32] Lowson, M., "The sound field for singularities in motion," *Proceedings of the Royal Society of London. Series A. Mathematical and Physical Sciences*, Vol. 286, No. 1407, 1965, pp. 559–572.